

Recapitulating Solid Stress on Tumor on a Chip for Nanomedicine Diffusive Transport Prediction

Alberto Martín-Asensio, Sergio Dávila, Jean Cacheux, Agnieszka Lindstaedt, Alicja Dziadosz, Darius Witt, Macarena Calero, Igor Balaz, and Isabel Rodríguez*

The characteristic mechanical forces at play within tumors include the abnormal solid and fluid stresses. These, together with the increased extracellular matrix (ECM) stiffness, are the major transport barriers affecting the nanomedicine delivery to solid tumors. Due to the elevated pressure within the tumor microenvironment, the transport of nanomedicines through the interstitial space is limited to diffusion. While this particular scenario is central for nanomedicine delivery to solid tumors, it has not been modeled *in vitro* before. To this end, herein, a tumor-on-a-chip microfluidic device is developed that is capable of recapitulating the solid stress scenario in tumors. This is achieved by integrating a pneumatic actuation to apply compression to the enclosed hydrogel ECM filling medium. Transport studies of model nanoparticles (NPs) across this medium are performed to determine their diffusion. For these NPs, it is demonstrated that their transport is drastically reduced by 65% due to the compression of the ECM gel matrix, reducing its pore size, with only an applied pressure of ≈ 4 Pa. The results obtained show that the actuated tumor-on-a-chip device can be used to evaluate the diffusive penetration capability of nanomedicines within a mechanical-constrained microenvironment such that of tumors.

1. Introduction

Nanotechnology has emerged as a promising tool for the early diagnosis and treatment of cancer.^[1–3] During the past decades, several nanotechnology-based therapies have been approved for clinical use.^[4] However, the success rate of nanomedicines entering clinical trials is extremely low.^[5–7] There is also a great number of nanomedicines being developed that show high efficacy in studies *in vitro*, yet they fail at *in vivo* tests.^[8,9] Thus, new more


advanced preclinical models with improved predictive value are required to be able to advance the clinical translation of nanomedicines. In this regard, tumor-on-a-chip (ToC) microfluidic devices are new testing platforms with greater physiological relevance than the traditional 2D cell cultures. They are capable of recapitulating key physiological aspects of the tumor microenvironment, like perfused 3D cellular microenvironments, allowing for the dynamic tuning of the physicochemical parameters.^[9–13] As such, these devices may provide more clinically relevant models to study the transport process of nanomedicines across the biological barriers for a better prediction of their *in vivo* performance.^[14,15]

During the recent years, several ToC devices have been developed as *in vitro* models to investigate different processes of the tumor biology. ToCs have been used to get a better understanding of cancer progression and metastasis,^[16–20] as well as angiogenesis and blood vessel formation.^[21–24] ToC devices have been also developed for the evaluation of new therapeutic approaches against cancer, including nanomedicines.^[25–28]

However, up-to-date, ToC devices have failed to model some of the main critical components involved in nanomedicine delivery to the tumor site. During the tumor delivery process, nanomedicines need to leave the bloodstream, penetrate into the interstitial tumor matrix and, ultimately, into the tumor cells. Here,

A. Martín-Asensio, S. Dávila, J. Cacheux, I. Rodríguez
IMDEA Nanoscience Institute
28049 Madrid, Spain
E-mail: i.rodriguez@imdea.org

A. Lindstaedt, A. Dziadosz, D. Witt
ProChimia Surfaces Sp. z o.o.
81-451 Gdynia, Poland

 The ORCID identification number(s) for the author(s) of this article can be found under <https://doi.org/10.1002/anbr.202200164>.

© 2023 The Authors. Advanced NanoBiomed Research published by Wiley-VCH GmbH. This is an open access article under the terms of the Creative Commons Attribution License, which permits use, distribution and reproduction in any medium, provided the original work is properly cited.

DOI: 10.1002/anbr.202200164

M. Calero
Department of Physical Chemistry
Complutense University of Madrid
28040 Madrid, Spain

M. Calero
Translational Biophysics
Hospital Doce de Octubre, Health Research Institute (imas12)
28041 Madrid, Spain

I. Balaz
Laboratory for Meteorology, Physics, and Biophysics
Faculty of Agriculture
University of Novi Sad
21000 Novi Sad, Serbia

an effective therapeutic action is achieved depending on whether the sufficient intratumoral accumulation of nanomedicine is reached.^[29–31]

Currently, evidences indicate that nanomedicines are unable to efficiently overcome the existing biological and biophysical barriers for drug delivery.^[32] These include the abnormal tumor vascularization and the mechanical forces that operate within the tumor, namely, the solid stress and interstitial fluid pressure, as well as the dense and heterogeneous structure of the extracellular matrix (ECM) that typically hinders nanoparticle (NP) permeation.^[1,33] The increased solid stress is caused by the rapid proliferation of neoplastic cells and the accumulation of structural components, such as proteins and cancer-associated fibroblasts. This accumulation produces a substantial stress to the adjacent tissue, which causes the constriction and even collapse of the tumor microvasculature, reducing the blood perfusion rates. At the same time, the lymphatic vessels are also constricted, reducing the clearance of excess fluids, which in turn increases the interstitial fluid pressure (IFP). The solid stress causes a compression of the ECM, which produces substantial interstitial hindrance to nanomedicine diffusive transport.^[29,33–37] In this situation of elevated interstitial fluid pressure and compressed ECM, the possibility for convective nanomedicine transport is prevented. The process of NP extravasation from the bloodstream is also affected by the elevated pressure within the tumor microenvironment. This process has been generally ascribed to the enhanced permeability and retention (EPR) effect that is, the preferential extravasation of NPs at the tumor site due to the enhanced permeability of the leaky tumor vasculature.^[38,39] Similarly, the EPR effect would rely just on diffusive transport rather than on the much more efficient convective transport.

Recently, researchers have begun to use ToC devices to study *in vitro* some of these NP transport processes,^[9,38] particularly the process of extravasation from artificial vessels^[39,40] and penetration through ECM^[41,42] or into tumor spheroids and organoids.^[43,44] However, how the abnormal solid and fluid stresses, together with the compression of the ECM, affect the NPs diffusive transport within the tumor microenvironment remains unaccounted for, despite that this aspect is critical for nanomedicine tumor delivery and therapeutic efficacy.

In this work, we present a ToC model that recreates *in vitro* the tumor's solid stress and related matrix compression. This is achieved by engineering a microfluidic platform that includes a vascular microchannel and two adjacent compartments at the sides. The microchannel and side compartments are separated by an array of micropillars closely positioned to hold within the compartments a hydrogel that acts as the ECM. A pressure cavity simulating a growing tumor is placed in each compartment. They are separated by a thin semicircular flexible membrane where controlled pneumatic pressure is applied. Using this ToC model, the diffusive transport of two model NPs is evaluated to determine the influence of solid stress and related gel matrix compression on the NP permeation hindrance.

This ToC device serves as an early demonstration of the tumor microenvironment for nanomedicine screening incorporating a variable tumor solid stress.

2. Experimental and Theoretical Calculations

2.1. COMSOL Simulation of Matrigel Compression

The ToC was specifically designed to recreate *in vitro* the tumor solid stress that is exercised on the surrounding ECM.^[45,46] The device includes a central channel (18 mm long and 60 μm wide) emulating a blood capillary connected by a porous wall to two adjacent lateral compartments that hold Matrigel as ECM. In these compartments, pressure is controllably applied by pneumatically actuating a 50 μm thick polydimethylsiloxane (PDMS) semicircular membrane that separates the tumor ECM compartment from the pressure cavity. This pressurized membrane simulates a growing tumor of approximately 1 mm in diameter. The membrane is positioned 100 μm apart from the central capillary and in this area, where the gel is compressed, the nanoparticle diffusive transport from the capillary and penetration into the Matrigel is studied.

Prior to the construction of the ToC devices, simulations were performed to estimate how the externally applied pressure is transmitted to the Matrigel. Solid mechanics simulations were performed by COMSOL Multiphysics (v.5.3a) using the fluid-structure interaction module. The parameters used were: PDMS Young's modulus $E = 400$ kPa, Matrigel concentration 8–11 mg mL^{-1} , and $E = 440$ Pa.^[47] For actuation, a pneumatic pressure of 1.3 kPa was applied onto the PDMS membrane. This pressure level was chosen arbitrarily in the midrange of the pressure controller.

To simulate the Matrigel compression, the fluid and matrix properties node was used to define the porous matrix properties, using values for permeability $K = 1.52 \times 10^{-14} \text{ m}^2$, dynamic viscosity $\mu = 932$ cP, and porosity $p = 1.2\%$ (see below Section 2.7).^[48] Outlet boundaries were set at the Matrigel borders, and a hydrostatic pressure of 16.9 Pa was established to simulate a 5 mm height Matrigel column at the chambers' end.

2.2. Hydrostatic Pressure Estimation

Because PDMS is a gas permeable material, air molecules from the externally applied pneumatic pressure to actuate the membrane could permeate and generate a hydrostatic pressure at the boundary between the PDMS membrane and the Matrigel. Hence, it was considered as a possible extra force compressing the gel matrix and interfering with the observed NP diffusion.^[49,50] To evaluate this possible effect, the hydrostatic pressure arising from gas permeation across the PDMS membrane was estimated (see Supporting Information). The calculation indicates that the generated hydrostatic pressure at the Matrigel-PDMS boundary was approximately equal to that applied at the central capillary for driving the flow. Hence, since there is no appreciable pressure drop across the Matrigel, no gel compression or convection is expected from this effect.

2.3. Microfluidic Device Fabrication

A micromachining process, including the steps of laser photolithography and plasma reactive ion etching (RIE), was implemented to fabricate the silicon masters as described before.^[51]

For this, 3" silicon wafers (Test grade, University Wafers) were first cleaned by oxygen plasma ($150 \text{ mL} \cdot \text{min}^{-1}$) for 5 min at 400 W (Tepla 600, PVA TePla AG). A primer was then applied by spin coating for 1 min at 2000 rpm. The wafers were then baked for 2 min at 120°C to evaporate the residual solvent. Then, a positive photoresist (AZ1512, Microchemicals) was spin coated at 1000 rpm to form a $2 \mu\text{m}$ thick film, followed by a baking step at 90°C for 1.5 min. After resist rehydration for 10 min, light exposure by a maskless laser writer (Heidelberg, DWL 66+, 405 nm) was used to write the microchannels onto the positive photoresist. The exposed substrate was developed (AZ351B, Microchemicals) for 1 min. In this process, the exposed resist was dissolved leaving openings according to the exposed patterns. Subsequently, silicon micromachining was carried out by cryogenic inductively coupled plasma RIE (ICP-RIE) (Oxford) based on fluorine gas. The optimized process parameters include a reactive gas flow of 19 sccm SF_6 , 5 sccm O_2 with a forward power of 15 W, and an ICP power of 275 W at 30 mTorr of pressure and at a temperature of -185°C . These parameters lead to an etch rate of $5 \mu\text{m} \cdot \text{min}^{-1}$.

The obtained silicon master mold was then replicated to produce the working molds before replicating them to finally obtain the working devices. Thermal nanoimprint lithography (TNIL) was used to imprint the master mold into an intermediate polymer stamp (IPS), producing a negative replica of the mold with semicircular profile. The TNIL was carried out at a temperature of 150°C and two pressure steps: 20 bars for 1 min and 40 bars for another minute using a NIL equipment (EITRE, Obducat). The master mold was coated with an antisticking layer (perfluorodecyltrichlorosilane, Strem Chemicals) at 70°C under vacuum overnight prior to the thermal imprint process to reduce adhesion. This is an essential step to facilitate the separation and to avoid breakage of the small structures while demolding. Finally, the IPS working molds were replicated with PDMS (Sylgard 184 Silicone Elastomer Kit, Dow) to produce the working copies. The reagents were mixed with a base-to-curing agent ratio of 10:1, poured onto the IPS mold, and cured for 60 min at 70°C . After peeling off the cured PDMS from the mold, holes were drilled using a 1.25 mm puncher (Kai Medical) for access to the central channel and pressure compartments. The ECM cavities access holes were made using a 3 mm puncher (Kai Medical). To make the final devices, sealing of the PDMS with a thin microscope cover glass (VWR, ECN 631-1574) was done by after activating the surfaces with oxygen plasma (O_2 rate of $150 \text{ mL} \cdot \text{min}^{-1}$ during 1 min at 50 W) (Tepla 600, PVA TePla AG).

The silicon master mold, IPS and PDMS copies were imaged by scanning electron microscopy (SEM) (Zeiss Sigma Vp FE-SEM) operating at 1.5 keV and an aperture of $7 \mu\text{m}$. Silicon master mold, IPS and PDMS channels geometrical parameters were characterized using a Dektak profilometer with a stylus force of 1 mg.

2.4. Synthesis of Fluorescent Gold Nanoparticles

$\text{HAuCl}_4 \cdot 3\text{H}_2\text{O}$ (100 mg, 25×10^{-5} mol) (Alfa Aesar, cat no. 12 325) was placed in a 250 mL flask and dissolved with methanol (30 mL) (Chempur, cat no. 116 219 904). In another flask, $\text{HSC}_{11}\text{EG}_6\text{OCH}_2\text{COOH}$ (132 mg, 25×10^{-5} mol) (Prochimia Surfaces, cat no. TH 003-m11.n6), water (20 mL), and acetic acid (1 mL) (Chempur, cat no. 115 687 607) were mixed. This solution

containing $\text{HSC}_{11}\text{EG}_6\text{OCH}_2\text{COOH}$ was added to the gold salt solution under stirring. The mixture turned from yellow to orange. NaBH_4 (97.5 mg, 257×10^{-5} mole) (Sigma-Aldrich, cat no. 21 3462) dissolved in water (6.6 mL) was added to the $\text{Au-SC}_{11}\text{EG}_6\text{OCH}_2\text{COOH}$ solution by stirring at room temperature. The solution color turned to brown. After 1 h of vigorous stirring, the aqueous hydrochloric acid solution (1 mL, 1 M) (Chempur, cat no. 115 752 837) was added. After the partial removal of the solvent under reduced pressure, acetone was added. The white suspension was separated from the black residue and centrifuged. The precipitate was dried under reduced pressure and dispersed in an aqueous solution of sodium hydroxide (5 mL, 0.01 M NaOH) (POCH S.A., cat no. BA0981118).

EDCI (159 mg, 102×10^{-5} mol) (Sigma-Aldrich, cat no. E7750) and sulfo-NHS (65 mg, 30×10^{-5} mol) (Sigma-Aldrich, cat no. 56 485) in water were added to 5 mL of gold nanoparticles functionalized with $\text{HSC}_{11}\text{EG}_6\text{OCH}_2\text{COOH}$. After 90 min of incubation, the pH was adjusted to 8.6 prior to the addition of an aqueous solution of cyanine5 amine (0.85 mg, 1.3×10^{-6} mol) (Lumiprobe, cat no. 430C0). The mixture was left for 15 min under stirring at room temperature and then at 4°C overnight.^[52] The crude product with a targeted 4% content of Cy5 dye on the surface was purified by dialysis against water pH 5.0 (MWCO: 3.5 kDa) (Serva, cat no. 44559.01). The dialysis bath was changed three times (after 6, 24, and 48 h). Finally, gold nanoparticles were centrifuged on Amicon columns (MWCO: 10 kDa) (Merck Millipore, cat no. UFC801024) and further characterized.

2.5. Nanoparticle Characterization

The synthesized 2.5-Cy5-AuNPs and the commercial 25 nm Micromer-redF NPs (Micromod Partikeltechnologie GmbH, 30-00-251) were characterized by means of dynamic light scattering (DLS) (Malvern Zetasizer Nano ZS) and transmission electron microscopy (TEM) (JEOL JEM 1400) to determine their ζ -potential, size distribution, and adsorbed protein corona when immersed in biological media.^[53–55]

To determine the NPs size by DLS, measurements were performed using the backscattered light detection from the dispersed sample. Nanoparticle concentrations of 1×10^{10} NPs mL^{-1} were prepared in MiliQ grade water, and the dispersions were stabilized for 60 s prior to the measurements at 25°C . Three readings were performed per sample with 15 runs per reading.

Measurements by TEM were performed by placing an $8 \mu\text{L}$ sample of the NP dispersion on a microscope grid, which was then left at room temperature for 30 s to let the NPs deposit on the grid. The excess was cleaned by placing the grid on a MiliQ water droplet for 30 s. The grid was subsequently dried at room temperature for 1 min. This cleaning step was performed twice. Finally, TEM images were acquired (JEOL JEM 1010).

The formation of a protein corona was realized by dispersing a NPs concentration of $\approx 1 \times 10^{14}$ NPs mL^{-1} in Dulbecco's Modified Eagle Medium (DMEM), low glucose (Biowest, L0060-500) complemented with 10% fetal bovine serum (FBS) (Sigma-Aldrich, F2442-50 mL), 1% L-glutamine (Biowest, X0550-100), and 1% penicillin-streptomycin (Gibco 15 140 122).

The resulting dispersion was incubated at 37 °C for 24 h prior to the TEM measurements. For this, 8 μL of the NP dispersion was deposited on a microscope grid and dried. Afterward, the grid with the sample was dipped for 1 min in uranyl acetate (UA) at 2% in water to act as a contrast agent.^[55] The collected TEM images were used to measure the NPs sizes using Fiji/ImageJ (v.1.53c), at least 250 NPs were measured. The image data collected for the 2.5-Cy5-AuNPs were fitted to a bimodal distribution, and that of the 25 nm micromer-redF NPs was fitted to a monomodal distribution following equations

$$\text{Monomodal: } \gamma = A \cdot e^{-\frac{(x-\mu)^2}{2\sigma^2}} \quad (1)$$

$$\text{Bimodal: } \gamma = A_1 \cdot e^{-\frac{(x-\mu_1)^2}{2\sigma_1^2}} + A_2 \cdot e^{-\frac{(x-\mu_2)^2}{2\sigma_2^2}} \quad (2)$$

where A is the peak height, μ is the mean value, and σ is the standard deviation. All fittings were performed using Python (v.3.8/Spyder IDE v.4.1.5).

The polydispersity index (PDI) for both DLS and TEM measurements was calculated as

$$\text{PDI} = \left(\frac{\sigma}{\mu}\right)^2 \quad (3)$$

where σ is the size standard deviation and μ is the mean diameter.^[56]

The diffusion coefficient of the nanoparticles in water was calculated using Stokes–Einstein equation

$$D = \frac{k_B \cdot T}{6\pi\eta(T)r} \quad (4)$$

Where k_B is the Boltzmann constant, T is the temperature, η is the dynamic viscosity, and r is the nanoparticle radius. To obtain the dynamic viscosity of water, the `iapws.iapws97` Python module was used.^[57] The Péclet number was used to establish if the diffusion was the predominant driving force and it was calculated as^[58,59]

$$Pe = \frac{\nu L}{D} \quad (5)$$

where ν is the flow velocity, D is the diffusion coefficient, and L is the characteristic length, which in this case was taken to be 100 μm since it is the distance from the central capillary to the PDMS actuated membrane.

2.6. Extracellular Matrix Characterization

To characterize Matrigel's porosity (8–11 mg mL⁻¹, Corning), a 5 μL sample was placed in a cover glass and kept at 37 °C for 30 min. Upon gelation, the sample was fixed with 2% paraformaldehyde (PFA) (95%, Sigma-Aldrich) and rinsed with H₂O MiliQ for 10 min at room temperature. Then, the sample was frozen using liquid N₂ and dry-frozen at -80 °C and ≈10⁻⁶ mbar of pressure for 48 h (LYOQUEST-85 PLUS, Telstar). Finally, the sample was sputter coated with 5 nm of gold (Leica EM ACE 600, Leica Microsystems) and images were taken using SEM (FE-SEM, ZEISS SIGMA VP, Carl Zeiss), operating at 5 keV with an aperture of 7 μm. The SEM images

were subsequently analyzed using a custom-made Python script. Three independent images were binarized using a thresholding method based on the triangle algorithm, implemented in the Python's `filters` module.^[60,61] Finally, the porosity was calculated as the area of pores (black pixels) over the total area.^[62]

The rheological properties of the Matrigel were measured using the Discovery RH-2 Rheometer (TA Instruments). The shear experiment was made with a conical plate and the software used was `Trios` (TA instruments). The relation between the mechanical properties with the temperature was made with the ramp protocol: first, the Matrigel sample was heated from 10 to 40 °C, and then, it was cooled from 40 to 10 °C. The control of temperature was made with a thermostat. The strain was set at 1% and the frequency at 1 Hz. The viscosity obtained was calculated from the loss modulus as $\eta = G''/(2\pi) \times 1000$ (mPa s).

The heating curve was fitted to a sigmoid function using the following expression

$$\eta = \eta_0 + \frac{L}{1 + e^{-k \cdot (T - T_0)}} \quad (6)$$

where η is the viscosity, η_0 is the initial viscosity before the heating process, L is related to the higher asymptote, k is the growth rate, and T_0 is the inflection point. Viscosity at 37 °C was calculated as the mean value of the cooling and heating ramps.

2.7. Nanoparticle Diffusion in Matrigel

To determine the NP diffusion in the Matrigel filled into the ToC device under flow and pressure conditions, the following procedure was implemented. Prior to filling, 10 mg mL⁻¹ solution of albumin-fluorescein isothiocyanate conjugate (A-FITC) (Sigma-Aldrich) was prepared and mixed with Matrigel in a 1:30 ratio to allow for visual inspection of the gel homogeneity after filling into the chip. The solution was kept at 4 °C to prevent gelation and 10 μL was introduced into the gel cavity by application of a negative pressure, while blocking the rest of the inlets of the device. Then, the corresponding reservoirs were filled with 30 μL of Matrigel and the device was left on ice for 15 min to allow filling by hydrostatic pressure the ECM compartments. Afterward, the device was incubated at 37 °C for 20 min to allow for the gelation of the Matrigel. Then, the device was placed at 4 °C in a humid environment for 24 h to prevent the gel dehydration. Subsequently, the ToC device was placed on a microscope heating plate at 37 °C (H601-K-frame-metal/glass, Okolab). The central capillary channel was filled with 1 × phosphate-buffered saline (PBS) (Alfa Aesar) and a constant flow at 23 mbar was kept for 10 min using a microfluidic flow controller (MCFS-EZ, Fluigent) to thoroughly rinse the channel.

The NP penetration experiments were carried out at vascular flow simulated conditions. For this, a NP dispersion of concentration ≈10¹⁴ NPs mL⁻¹ was prepared in a solution of 1 × PBS, 1% bovine serum albumin (BSA) (w/w), and Xanthan gum at a concentration of 0.066 (g L⁻¹) (abcr GmbH) to make a blood analog fluid, as described by van der Broek et al.^[63] This NP dispersion was injected into the central channel by applying a 23 mbar pressure drop across the channel, which was maintained during the whole experiment. Diffusion of the NPs into the Matrigel was

studied under different pressurized conditions by applying an external pneumatic pressure of 0, 7, or 13 mbar through the pressure cavities onto the lateral compartments. The temperature was maintained constant at 37 °C for the duration of the diffusion study using a heated plate.

2.8. Image Analysis to Determine Diffusional Permeability

Image acquisition was performed using an epifluorescence microscope (Leica DMi8, Leica Microsystems) coupled to a camera (Orca Flash 4.0 V3, Hamamatsu). Once a fluorescence signal of the NPs was detected in the central channel, images were acquired using ImageJ Micromanager (v.1.4.22) at time intervals of 10, 30, or 60 s and magnifications of 20 or 40 \times .^[64] Images were then analyzed using a purposely written Python script. Regions of interest (ROI) were selected in the Matrigel compartment and in the central channel for analysis. The permeability coefficient was obtained using the following equation:^[39,40]

$$P = \frac{A \cdot (I_f - I_{t=0})}{w_p \cdot \Delta t \cdot (I_c - I_p)_{t=0}} \quad (7)$$

where A is the ECM ROI's area, $I_{t=0}$ and I_f are the ECM ROI's total fluorescence intensity at $t = 0$ and at the end of the experiment, respectively, w_p is the pillars ROI's width across which diffusion takes place, Δt is the total experiment time, I_c is the central channel ROI's total fluorescence at $t = 0$, and I_p is the pillars ROI's total fluorescence at $t = 0$. The diffusion coefficient was obtained from the permeability using the following relationship^[65]

$$D = P \cdot l \quad (8)$$

Where P is the permeability coefficient calculated using Equation (7), l is the pillars' length.

3. Results and Discussion

3.1. Microfluidic Device Design and Simulation

The ToC device (Figure 1a) was designed to recreate some of the structural and biomechanical components of the in vivo tumor microenvironment as an in vitro model for the evaluation of nanomedicine transport characteristics. Particularly, the ToC device was engineered to incorporate a tunable pressure actuation to artificially recreate the solid pressure that a growing tumor would apply to the surrounding ECM.^[33,45] The ToC design includes a central capillary of 60 μm in width and semicircular profile in communication with two lateral compartments that hold Matrigel, used in this case as ECM.^[66] These compartments are connected to the central capillary by a linear array of 10 μm pillars closely positioned, leaving gaps of 10 μm to prevent the Matrigel from entering the central capillary. To apply pressure to the ECM, two pressure cavities were placed at a distance of 100 μm from the central capillary. They are separated from the ECM compartments by flexible PDMS membranes of 50 μm in width with an external diameter of 1 mm.

Figure 1b shows the 3D COMSOL simulation results for the PDMS membrane deflection obtained upon the application of

13 mbar (1.3 kPa) pneumatic pressure to the cavity. The simulation (Figure 1d) indicates that the pressure applied to the Matrigel decreases as the distance to the membrane increases, with the maximum pressure being approximately 4 Pa. This pressure level achieved with the device is in fact ≈ 10 times lower than that reported for in vivo solid tumors.^[46] Nonetheless, it serves the main purpose of this study in demonstrating the impact of solid pressure on the diffusive transport of NPs through extracellular gel media.

The flow profile at the central capillary of the ToC was simulated (Figure S1a, Supporting Information) indicating that, for the pressure applied, a laminar flow was obtained in the central capillary with the characteristic parabolic profile (Figure S1b, Supporting Information), presenting an average and maximum fluid flow velocity of $\bar{v} = 0.59 \text{ m s}^{-1}$ and $v_{\text{max}} = 0.95 \text{ m s}^{-1}$, respectively. These values were not significantly affected by the pneumatic pressure applied onto the gel compartment. The possible impact of a convective flow within the Matrigel fibers derived from pressure drop across the gel was also assessed. The estimated flow velocity values obtained from the simulations, as shown in Figure 1e, are in the range of tenths of nm s^{-1} . These values are seven orders of magnitude lower than those in the central capillary and, as such, it is estimated that the convective transport will not be significant compared to the diffusive transport of the NPs. For a point situated at the center of the gel compartment and close to the PDMS membrane, the calculated interstitial flow velocity revealed an insignificant increase from 35.2 to 36.1 nm s^{-1} when a pressure of 13 mbar was applied.

3.2. Microfluidic Tumor-On-a-Chip Device Fabrication

The microfluidic device fabrication process is shown in Figure 2a. The silicon master mold structure was first obtained after the lithography and ICP-RIE process (Figure S2a, Supporting Information). The master was imprinted into an IPS material obtaining the negative relief of the required structure (Figure S2b, Supporting Information). This intermediate substrate was replicated into PDMS via soft lithography. In the PDMS copy (Figure 2b), these pillars presented a $10 \times 20 \mu\text{m}$ rectangular shape with $\approx 30 \mu\text{m}$ in height. The central capillary showed a 30 μm radius semicircular structure, which is in the range of tumor vessels.^[67,68] The PDMS membranes, where pneumatic pressure is applied, were $\approx 50 \mu\text{m}$ in width and $\approx 38 \mu\text{m}$ in height. They are placed 100 μm apart from the central capillary to follow similar distances as those found between the tumor cells and the blood microvessels.^[69,70] Profilometry measurements (Figure 2c) were performed at the different steps of the process to verify the fidelity of the replication.

3.3. Nanoparticle Synthesis and Characterization

Two different types of NPs with very different characteristics were used as model particles for diffusion measurements on the ToC device: 2.5 nm gold NP (2.5-Cy5-AuNPs) and 25 nm polymeric NPs (Micromer-redF-25 nm). The gold NPs (AuNPs) were synthesized with a small gold core to limit the

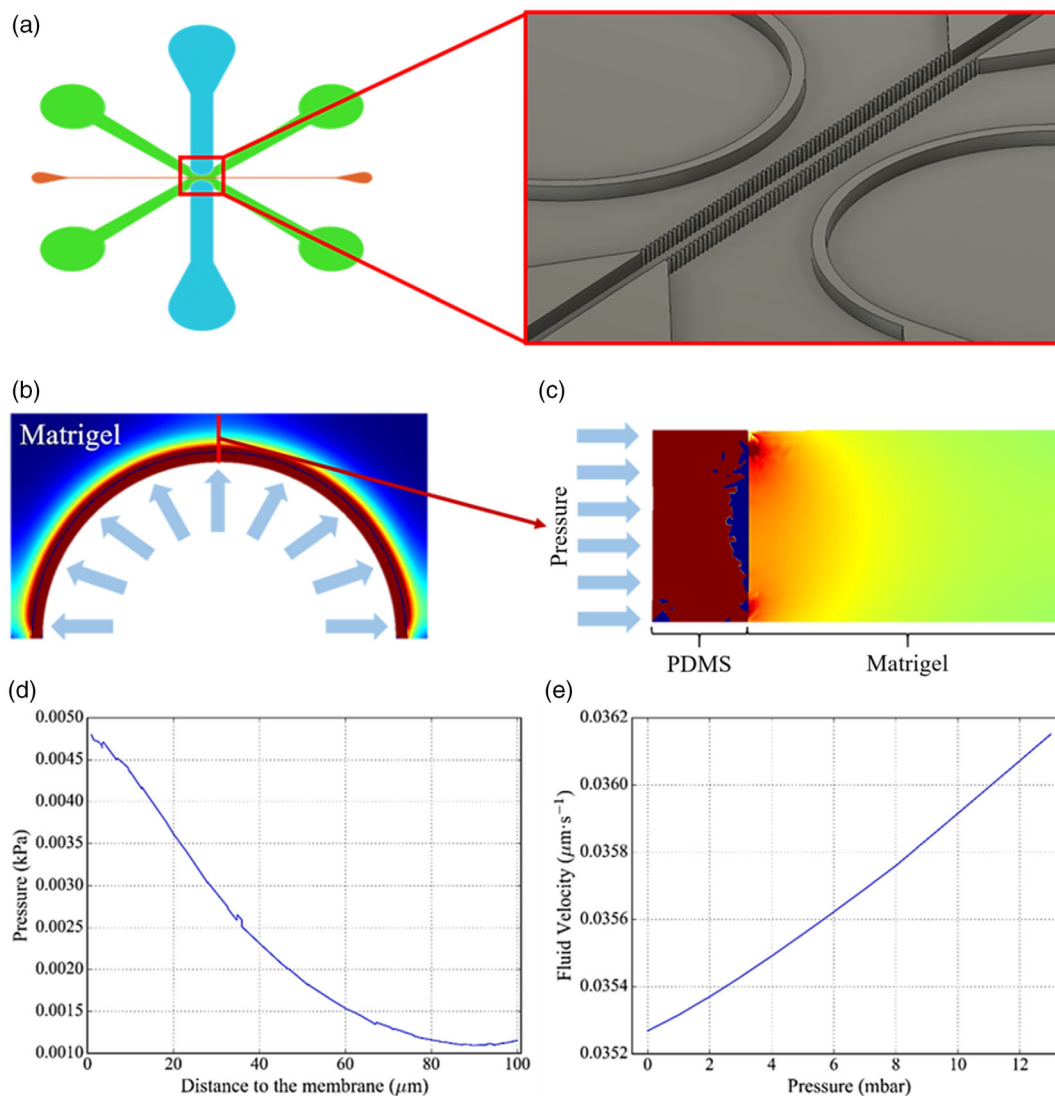


Figure 1. Design and simulation of the microfluidic device. a) Schematic of the microfluidic device. Pneumatic channels are shown in blue, ECM cavities in green, and the artificial blood capillary in orange. A scaled 3D drawing of the microfluidic structure is also shown in gray. b) Top view of the COMSOL Multiphysics simulation of 13 mbar of pressure applied to the PDMS membrane and pressure drop across the ECM. c) Lateral view of the simulation results. d) Pressure drop in the Matrigel obtained from the simulation due to the applied pressure to the PDMS membrane. e) Fluid velocity in the Matrigel as a function of the applied pressure to the membrane.

fluorescence signal quenching as it is required for tracking the NP diffusion. To stabilize the AuNPs dispersion and improve water compatibility, the AuNPs were first functionalized with undecanethiol-terminated hexaethylene glycol carboxylic acid (HSC11EG6OCH₂COOH). This ligand was also selected to act as a chemically suitable moiety to bind the Cy5 (sulfo-cyanine5) fluorescent dye by in situ coupling. The structure of an ultrasmall gold core with fluorescent dye on the surface is shown in Figure S3, Supporting Information.

TEM measurements of 2.5-Cy5-AuNPs dispersed in water (Figure 3a) indicated that the Au-NPs synthesis produced two NP populations with sizes centered at 2.05 ± 0.19 and 8.26 ± 2.63 nm, with relative concentrations of 92.3% and 7.7%, respectively. DLS measurements of the NPs hydrodynamic

diameter (Figure S4a) showed only one peak corresponding to a NP size distribution of 15 ± 3 nm (PDI = 0.04), suggesting that the smallest NP population was the predominant in the sample.

Since the diffusion of NPs will be measured in biological fluids such as cell culture media, the surface adsorption of proteins forming the so-called protein corona (PC) is an essential characterization to perform. The PC alters the size, charge, and aggregation state of the NPs in solution and, as such, it highly influences their transport properties.^[55,71] To estimate the size increase due to protein binding to the Au-NPs, TEM imaging using UA as contrast stain was performed. Figure 3c shows a TEM image where the two distributions of Au-NPs can be seen (colored green and orange for the 2.1 and 8.3 nm, respectively). Quantification of the distribution of the NPs size populations is

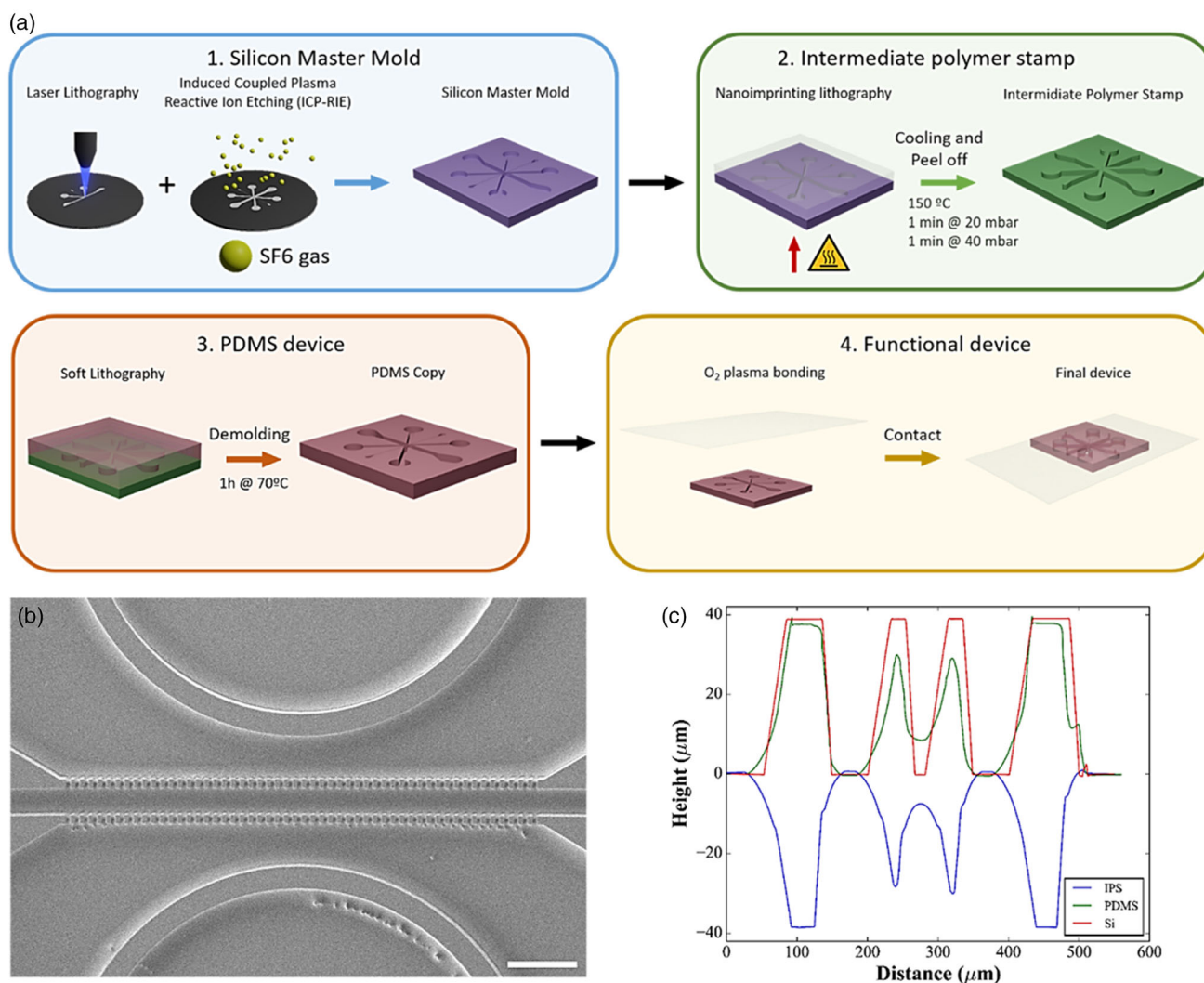


Figure 2. Fabrication of the PDMS ToC microfluidic device. a) Scheme of the fabrication process. The silicon master mold is obtained from a silicon wafer by optical lithography and ICP-RIE. Afterward, the intermediate polymer stamp (IPS) is obtained via NIL. Finally, the PDMS device is obtained by soft lithography and it is sealed with a microscope cover slide. b) Scanning electron microscope image of the PDMS device where the ToC's structure is shown. c) Profilometry measurements of the channels in the silicon master mold (red), IPS (blue), and PDMS (green).

displayed in the insert. Measurements of the NPs size prior acquiring the PC, that is the NP core and organic ligands, offered sizes of 11.9 ± 2.5 and 25.8 ± 4.3 nm for each of the sample populations (Figure S5a), being the smallest NPs the predominant population. After adsorption of the PC, the size of the NP populations increased to 31.6 ± 7.2 nm (PDI = 0.05) and 48.2 ± 6.6 nm (PDI = 0.02), respectively. This implies an increment of ≈ 20 nm for both populations. Measurements of the relative NP concentrations by TEM could not be performed reliably due to the background noise of the media. This made the identification of NPs difficult by image processing. Hence, the distribution was assumed to be similar to what was obtained before from the measurements in water.

The 25 nm micromer-redF NPs are made of a polymethyl methacrylate (PMMA) matrix with encapsulated rhodamine-B fluorophore molecules. Both TEM (Figure 3a, right) and DLS measurements (Figure S4b, Supporting Information) of water

dispersions showed a single population of NPs, with sizes of 28.2 ± 4.7 nm (PDI = 0.03) and 34.2 ± 10.7 nm (PDI = 0.1), respectively. The addition of UA (Figure S5b, Supporting Information) confirmed that no molecules were attached to the surface, since the TEM measurements furnished a similar size (31.3 ± 5.5 nm) as the measurements in plain water aforementioned. Measurements of the PC showed that the NP size increased to 50.2 ± 6.9 nm (Figure 3b, right), a similar increment as that was seen for the 2.5-Cy5-AuNPs. This substantial size increment in both types of NPs highlights the need to account for the PC for NPs transport studies in biological media, since both size and surface composition are significantly altered.^[53,72,73] **Table 1** summarizes the physicochemical properties of the NPs used in this study.

The size characterization data obtained were used to estimate the diffusion coefficient of the NPs in water using Equation (4), obtaining 20.7 ± 4.7 and $13.1 \pm 1.8 \mu\text{m}^2 \cdot \text{s}^{-1}$ for the 2.5-Cy5-AuNPs

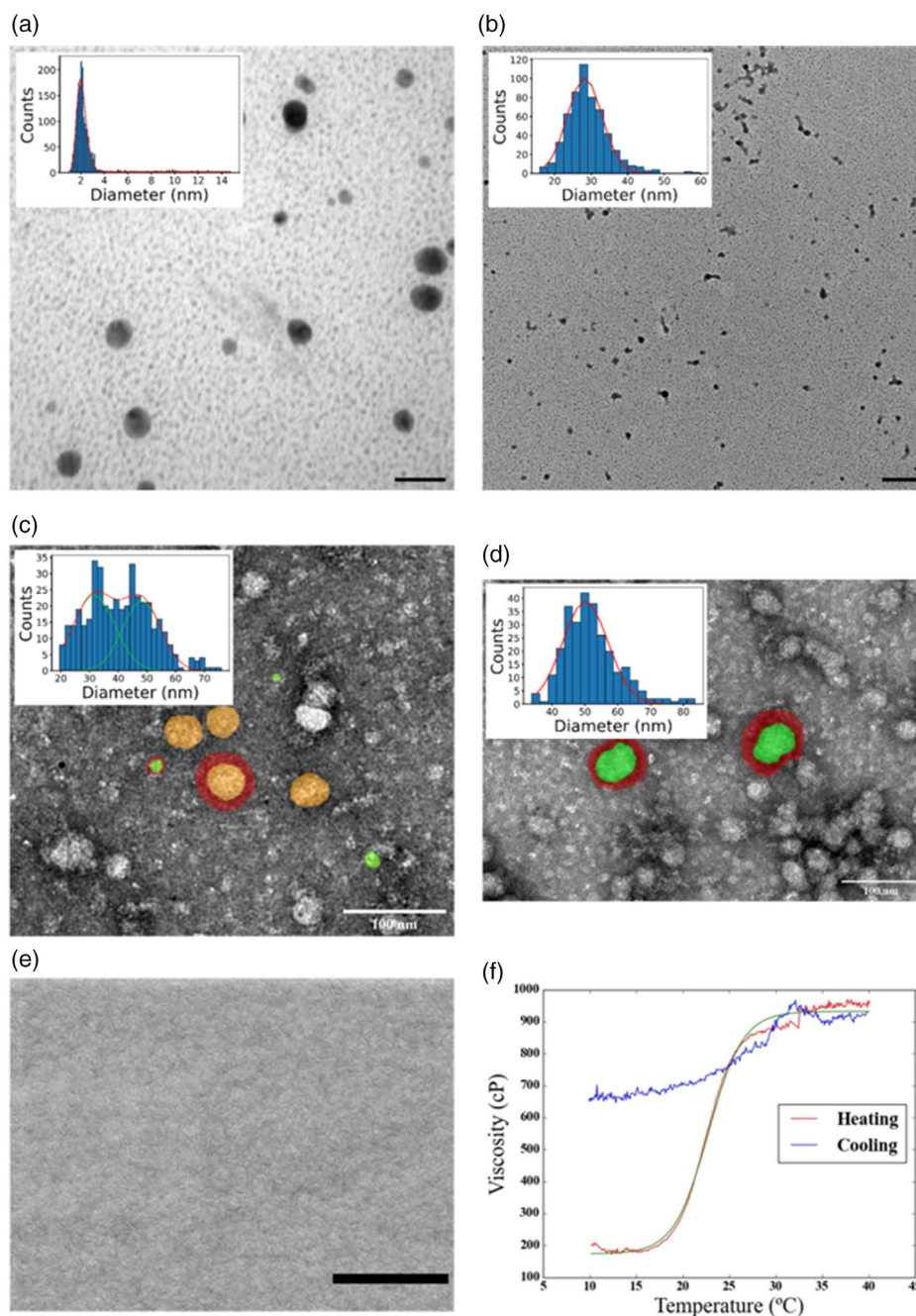


Figure 3. Characterization of the nanoparticles and extracellular matrix materials employed in this study. a) Transmission electron microscopy (TEM) images and measured size distributions of the 2.5-Cy5-AuNPs (scale bar: 20 nm). b) TEM images and measured size distributions of the 25 nm Micromer-redF dispersed in water (scale bar: 200 nm). c) TEM images and measured size distributions of the 2.5-Cy5-AuNPs dispersed in DMEM and marked with UA (scale bar: 100 nm). d) TEM images and measured size distributions of the 25 nm Micromer-redF dispersed in DMEM and marked with uranyl acetate (scale bar: 100 nm). e) Scanning electron microscopy (SEM) image of Matrigel deposited in a cover glass (scale bar: 3 μ m). f) Matrigel rheometry measurements during heating and cooling ramps.

and 25 nm micromer-redF NPs, respectively. These results indicate that diffusion would be a main driving force for these NPs transport, since the Péclet number (Equation (5)), calculated using the velocity values obtained from the COMSOL Multiphysics simulation, is lower than 0.3 for both nanoparticles.^[58,59]

The ζ -potential of both types of NPs dispersed in water was also measured using DLS obtaining values of -33 ± 2 and -28 ± 1 mV for 2.5-Cy5-AuNPs and 25 nm micromer-redF NPs, respectively. Since both NPs showed similar ζ -potential values, no differences in transport behavior among both types of NPs were expected due to charge.^[35,36,74]

Table 1. Physicochemical properties of the nanoparticles used in this study.

Nanoparticle	DLS [nm]		TEM [nm]		ζ -potential [mV]	Diffusion coefficient (in water) [$\mu\text{m}^2\cdot\text{s}^{-1}$]
	–	Without UA	With UA [NP]	With UA [NP + PC]		
2.5-Cy5-AuNPs	15 ± 3	2.1 ± 0.2	12.0 ± 2.5	31.6 ± 7.2	–33 ± 2	20.7 ± 4.7
Micromer-redF-25 nm	34 ± 11	28.2 ± 4.7	31.3 ± 5.5	50.2 ± 6.9	–28 ± 1	13.1 ± 1.8

3.4. Extracellular Matrix Characterization

Since the NPs diffusion is influenced by the porosity and dynamic viscosity of the Matrigel, these parameters were initially measured by SEM and rheometry. For this, a thin film of Matrigel was gelled over a glass cover. SEM images were taken to investigate the size of the pores formed. Figure 3e shows the dense gel layer formed with hardly visible, very small pores. Analysis of the images provided porosity values of $p = 1.2 \pm 0.3\%$, which are in the same order of magnitude as previous studies have reported, and within the expected batch-to-batch variability.^[40,75,76]

Measurements of the dynamic viscosity of the Matrigel as a function of the temperature were performed within the range of 10–40 °C during the heating and cooling ramps.^[65] To the best of our knowledge, Matrigel’s dynamic viscosity has only been reported for temperatures below 12 °C.^[77] The rheometry measurements performed are shown in Figure 3f and indicate that below 20 °C, the Matrigel viscosity is low, corresponding to nongelled state. As the temperature increases, its viscosity rapidly increases following a sigmoidal function. Fitting this ramp to Equation (6), returns a gel crosslinking rate constant $k = 0.54 \pm 0.01 \text{ } ^\circ\text{C}^{-1}$, an initial viscosity $\eta_0 = 173 \pm 6 \text{ cP}$, with an inflection point temperature $T_0 = 22.77 \pm 0.01 \text{ } ^\circ\text{C}$, which is

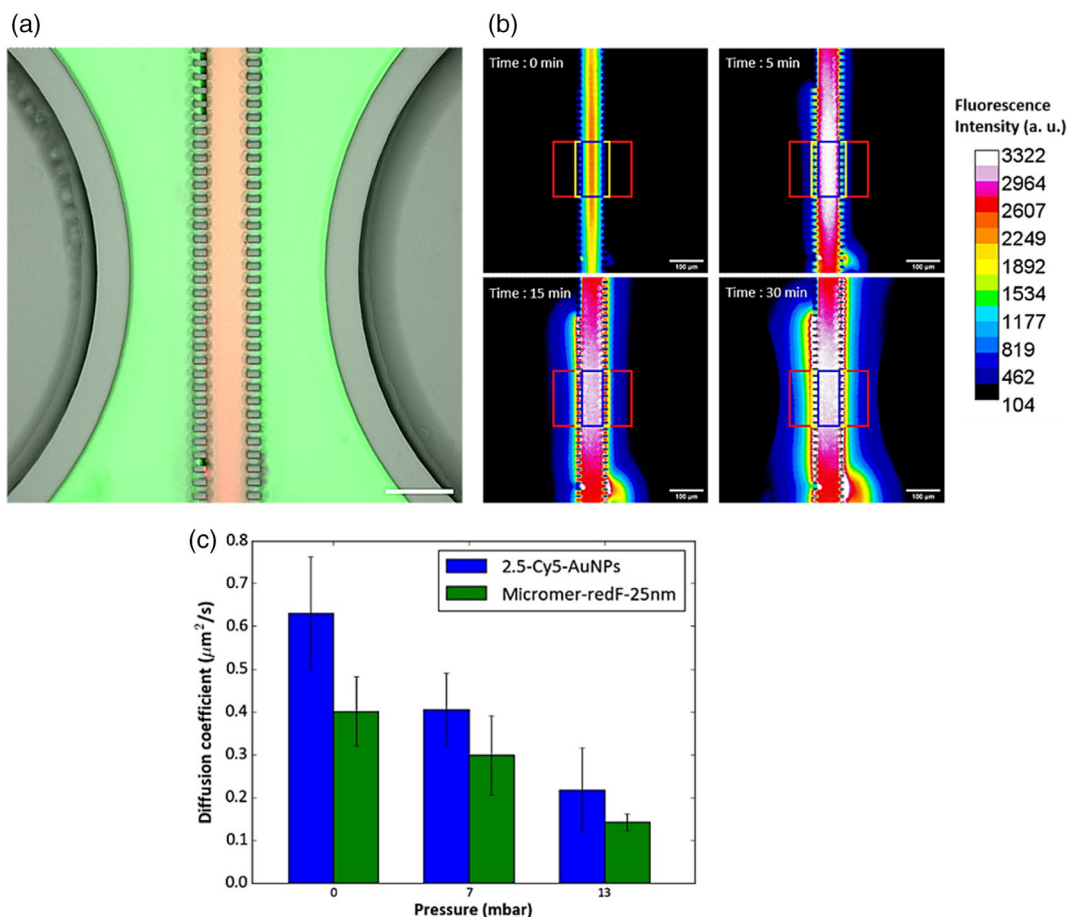


Figure 4. Study of nanoparticles diffusion into Matrigel. a) Compound image including a bright-field image of the ToC structure (gray), the FITC-marked fluorescence Matrigel (green), and the fluid of nanoparticles (orange) (scale bar: 100 μm). b) Time-lapse images of 2.5-Cy5-AuNPs diffusion into the Matrigel (scale bar: 100 μm). c) Diffusion coefficients of both types of NPs at different applied pressures. Values are presented as mean \pm standard deviation ($n \geq 3$). All results are statistically significant with $p < 0.05$.

within the temperatures range at which Matrigel gels.^[78] Measurements during the cooling process showed a slight decrease in viscosity. However, when cooled below the temperature inflection point, the Matrigel still showed a higher viscosity than that measured during the heating ramp, suggesting that the gelled cross-linked structure is preserved even if the gel is cooled down. At 37 °C, the cross-linked Matrigel presented a viscosity ($\eta = 932 \pm 19$ cP).

3.5. Nanoparticle Interstitial Diffusive Penetration into Matrigel

An optical image of a ToC device is shown in **Figure 4a**. This image shows that the Matrigel (**Figure 4a**, colored in green) is in contact with the central capillary where a constant NPs flow (**Figure 4a**, colored in red) is maintained. These cavities are separated by a linear micropillar array (**Figure 4a** in purple), which acts as a capillary barrier for the Matrigel due to the small size gap within the micropillars.

Representative time-lapse images of the NPs diffusion into the Matrigel are seen in **Figure 4b**, which displays the NPs fluorescence intensity differences as they diffuse out of the central capillary. ROI areas were selected to measure the NP fluorescent signal intensity in the Matrigel at the ECM compartment (ROI in red) or at the central channel (ROI in blue) or within the micropillars (ROI in yellow). By analyzing these images, the NP permeability was calculated as described in Section 2.8. The diffusion coefficient was then calculated from these data (**Table S1**, Supporting Information) using Equation (8), obtaining values of 0.63 ± 0.13 and $0.40 \pm 0.08 \mu\text{m}^2 \text{s}^{-1}$ for the 2.5-Cy5-AuNPs and 25 nm micromer-redF, respectively, without pressure actuation. These values were reduced to 0.22 ± 0.08 and $0.14 \pm 0.02 \mu\text{m}^2 \text{s}^{-1}$ when the pneumatic pressure of 13 mbar was applied to the PDMS membrane (**Figure 4c**). This represents a 65% reduction in the diffusive transport for the NPs under study. When the pressure of 7 mbar was applied, the reduction was $\approx 30\%$.

The results obtained without the pressure actuation are in accordance with those reported in the literature for NPs with similar properties.^[79] The values are much lower than those calculated theoretically in water using the Stokes–Einstein relation (Equation (4)). As expected, the diffusive motion of the NPs in the cross-linked Matrigel is very much delayed compared to their free diffusion in water due to the geometrical constraints imposed by the hydrogel mesh, and any possible electrostatic or hydrophobic interactions or specific binding events that may be taking place between the NPs and the Matrigel components.^[42]

The decrease in the measured diffusion coefficient due to the externally applied pneumatic pressure indicates that convective flows are not generated but instead, a fraction of the applied pressure is transmitted to the gel matrix. This pressure compresses the Matrigel causing a reduction on the pores formed by the hydrated network of protein fibers, which in turn causes an increased transport hindrance to the NPs diffusion.^[35,80]

Hence, the findings in this study provide experimental evidence on how the interstitial matrix compression reduces the NPs penetration. Starting from this, more advanced models can be created by more accurately recreating the tumor solid

stress level and or by including a more complex matrix components such as collagen and tumor-associated cells.

4. Conclusion and Outlook

A ToC device that can be actuated to recreate the tumor solid stress was developed as an in vitro model to examine and predict the diffusive transport of drug nanocarriers through the ECM. The device incorporates a central capillary, mimicking a tumor microvessel, with two adjacent extracellular tumor matrix compartments at the sides. The tumor solid stress is recreated by compressing the ECM compartment through a pneumatically actuated membrane.

The diffusive transport of two well-characterized NPs in biological media was studied to validate the ToC in vitro model. The device allowed to systematically investigate the diffusive transport hindering effect caused by the solid stress. A sharp decrease in diffusion of up to 65% was observed when 13 mbar of pressure was pneumatically applied.

The actuated ToC device proved to be a useful in vitro model of the tumor microenvironment, particularly interesting to recreate and study the influence of the tumor solid stress on the penetration of nanomedicines. Furthermore, the device supports the evidence that ECM compression is a major contributor of the diffusive hindrance for effective nanomedicine tumor delivery.^[33]

The ToC device can be incorporated with additional tumor microenvironment features such as endothelial barriers and tumor cells to have a more faithful scenario of the tumor microenvironment. These devices will provide for a more realistic model to obtain optimized design parameters for improved nanomedicine delivery.

Supporting Information

Supporting Information is available from the Wiley Online Library or from the author.

Acknowledgements

This work was performed within the framework of the EVONANO project funded by the European Union's Horizon 2020 FET Open program under grant agreement No. 800983 and partially funded by the "Severo Ochoa" Program for Centers of Excellence in R&D (MICIN, Grant CEX2020-001039-S). A.M.A. acknowledges a predoctoral scholarship from the Spanish Ministry of Science and Innovation Severo Ochoa Program for Centers of Excellence in R&D (grant no: PRE2019-88686). The authors greatly acknowledge the assistance for TEM imaging by the CBM-SO electron microscopy service staff.

Conflict of Interest

The authors declare no conflict of interest.

Data Availability Statement

The data that support the findings of this study are available from the corresponding author upon reasonable request.

Keywords

microfluidics, nanomedicine, organ-on-a-chip, solid tumors, tumor-on-a-chip

Received: November 21, 2022

Revised: January 31, 2023

Published online: April 28, 2023

- [1] R. K. Jain, T. Stylianopoulos, *Nat. Rev. Clin. Oncol.* **2010**, *7*, 11.
- [2] V. Wagner, A. Dullaart, A. K. Bock, A. Zweck, *Nat. Biotechnol.* **2006**, *24*, 10.
- [3] T. Sun, Y. S. Zhang, B. Pang, D. C. Hyun, M. Yang, Y. Xia, *Angew. Chem. Int. Ed.* **2014**, *53*, 46.
- [4] A. C. Anselmo, S. Mitragotri, *Bioeng. Transl. Med.* **2019**, *4*, 3.
- [5] L. Zhang, F. X. Gu, J. M. Chan, A. Z. Wang, R. S. Langer, O. C. Farokhzad, *Clin. Pharmacol. Ther.* **2008**, *83*, 5.
- [6] T. Van Dyke, *Nat. Med.* **2010**, *16*, 9.
- [7] J. M. Reichert, J. B. Wenger, *Drug Discov. Today* **2008**, *13*, 1.
- [8] S. Hua, M. B. C. de Matos, J. M. Metselaer, G. Storm, *Front. Pharmacol.* **2018**, *9*, 1.
- [9] G. Trujillo-de Santiago, B. G. Flores-Garza, J. A. Tavares-Negrete, I. M. Lara-Mayorga, I. González-Gamboa, Y. S. Zhang, A. Rojas-Martínez, R. Ortiz-López, M. M. Álvarez, *Materials* **2019**, *12*, 18.
- [10] E. W. Esch, A. Bahinski, D. Huh, *Nat. Rev. Drug Discov.* **2015**, *14*, 4.
- [11] Y. S. Zhang, Y. N. Zhang, W. Zhang, *Drug Discov. Today* **2017**, *22*, 9.
- [12] L. Wan, C. A. Neumann, P. R. Leduc, *Lab Chip* **2020**, *20*, 5.
- [13] D. J. Beebe, G. A. Mensing, G. M. Walker, *Annu. Rev. Biomed. Eng.* **2002**, *4*, 261.
- [14] H. F. Wang, R. Ran, Y. Liu, Y. Hui, B. Zeng, D. Chen, D. A. Weitz, C. X. Zhao, *ACS Nano* **2018**, *12*, 11.
- [15] M. N. Vu, P. Rajasekhar, D. P. Poole, S. Y. Khor, N. P. Truong, C. J. Nowell, J. F. Quinn, M. Whittaker, N. A. Veldhuis, T. P. Davis, *ACS Appl. Nano Mater.* **2019**, *2*, 4.
- [16] K. E. Sung, N. Yang, C. Pehlke, P. J. Keely, K. W. Eliceiri, A. Friedl, D. J. Beebe, *Integr. Biol.* **2011**, *3*, 4.
- [17] Y. Wang, D. Wu, G. Wu, J. Wu, S. Lu, J. Lo, Y. He, C. Zhao, X. Zhao, H. Zhang, S. Q. Wang, *Theranostics* **2020**, *10*, 1.
- [18] R. Portillo-Lara, N. Annabi, *Lab Chip* **2016**, *16*, 21.
- [19] A. Skardal, M. Devarasetty, S. Forsythe, A. Atala, S. Soker, *Biotechnol. Bioeng.* **2016**, *113*, 9.
- [20] S. Mi, Z. Du, Y. Xu, Z. Wu, X. Qian, M. Zhang, W. Sun, *Sci. Rep.* **2016**, *6*, 1.
- [21] W. J. Polacheck, M. L. Kutys, J. B. Tefft, C. S. Chen, in *Microfabricated Blood Vessels For Modeling The Vascular Transport Barrier*, Springer US, New York **2019**.
- [22] K. S. Ato, K. S. Ato, *Anal. Sci.* **2018**, *34*, 755.
- [23] S. Lee, J. Ko, D. Park, S. R. Lee, M. Chung, Y. Lee, N. L. Jeon, *Lab Chip* **2018**, *18*, 18.
- [24] H. Lee, W. Park, H. Ryu, N. L. Jeon, *Biomicrofluidics* **2014**, *8*, 5.
- [25] P. M. Valencia, O. C. Farokhzad, R. Karnik, R. Langer, *Nat. Nanotechnol.* **2012**, *7*, 10.
- [26] A. Albanese, A. K. Lam, E. A. Sykes, J. V. Rocheleau, W. C. W. Chan, *Nat. Commun.* **2013**, *4*, 2718.
- [27] B. Kwak, A. Ozcelikkale, C. S. Shin, K. Park, B. Han, *J. Control. Release* **2014**, *194*, 157.
- [28] M. R. Carvalho, D. Barata, L. M. Teixeira, S. Giselbrecht, R. L. Reis, J. M. Oliveira, R. Truckenmüller, P. Habibovic, *Sci. Adv.* **2019**, *5*, 5.
- [29] J. W. Nichols, Y. H. Bae, *Nano Today* **2012**, *7*, 6.
- [30] A. S. Mikhail, C. Allen, *J. Control. Release* **2009**, *138*, 3.
- [31] C. M. Lee, I. F. Tannock, *BMC Cancer* **2010**, *10*, 255.
- [32] S. Wilhelm, A. J. Tavares, Q. Dai, S. Ohta, J. Audet, H. F. Dvorak, W. C. W. Chan, *Nat. Rev. Mater.* **2016**, *1*, 5.
- [33] R. K. Jain, J. D. Martin, T. Stylianopoulos, *Annu. Rev. Biomed. Eng.* **2014**, *16*, 321.
- [34] L. Tomasetti, M. Breunig, *Adv. Healthcare Mater.* **2018**, *7*, 3.
- [35] T. Stylianopoulos, B. Diop-Frimpong, L. L. Munn, R. K. Jain, *Biophys. J.* **2010**, *99*, 10.
- [36] T. Stylianopoulos, M. Z. Poh, N. Insin, M. G. Bawendi, D. Fukumura, L. L. Munn, R. K. Jain, *Biophys. J.* **2010**, *99*, 5.
- [37] T. Stylianopoulos, V. H. Barocas, *Comput. Methods Appl. Mech. Eng.* **2007**, *196*, 31.
- [38] C. Tian, S. Zheng, X. Liu, K. i. Kamei, *J. Nanobiotechnol.* **2022**, *20*, 1.
- [39] Y. T. Ho, G. Adriani, S. Beyer, P. T. Nhan, R. D. Kamm, J. C. Y. Kah, *Sci. Rep.* **2017**, *7*, 1.
- [40] M. G. Barbato, R. C. Pereira, H. Mollica, A. L. Palange, M. Ferreira, P. Decuzzi, *J. Colloid Interface Sci.* **2021**, *594*, 409.
- [41] K. P. Valente, A. Suleman, A. G. Brolo, *ACS Appl. Bio. Mater.* **2020**, *3*, 10.
- [42] A. B. Engin, D. Nikitovic, M. Neagu, P. Henrich-Noack, A. O. Docea, M. I. Shtilman, K. Golokhvast, A. M. Tsatsakis, *Part. Fibre Toxicol.* **2017**, *14*, 1.
- [43] K. Huang, R. Boerhan, C. Liu, G. Jiang, *Mol. Pharm.* **2017**, *14*, 12.
- [44] V. Carvalho, M. Bañobre-López, G. Minas, S. F. C. F. Teixeira, R. Lima, R. O. Rodrigues, *Bioprinting* **2022**, *27*, e00224.
- [45] H. T. Nia, M. Datta, G. Seano, P. Huang, L. L. Munn, R. K. Jain, *Nat. Protoc.* **2018**, *13*, 5.
- [46] H. T. Nia, H. Liu, G. Seano, M. Datta, D. Jones, N. Rahbari, J. Incio, V. P. Chauhan, K. Jung, J. D. Martin, V. Askoxylakis, T. P. Padera, D. Fukumura, Y. Boucher, F. J. Hornicek, A. J. Grodzinsky, J. W. Baish, L. L. Munn, R. K. Jain, *Nat. Biomed. Eng.* **2017**, *1*, 1.
- [47] S. S. Soofi, J. A. Last, S. J. Lliensiek, P. F. Nealey, C. J. Murphy, *J. Struct. Biol.* **2009**, *167*, 3.
- [48] C. P. Ng, S. H. Pun, *Biotechnol. Bioeng.* **2007**, *23*, 1.
- [49] A. Lamberti, S. L. Marasso, M. Cocuzza, *RSC Adv.* **2014**, *4*, 106.
- [50] M. Johnson, G. Liddiard, M. Eddings, B. Gale, *J. Micromec. Microeng.* **2009**, *19*, 9.
- [51] S. Dávila, J. Cacheux, I. Rodríguez, *ACS Omega* **2021**, *6*, 39.
- [52] G. J. Sánchez, P. Maury, L. Stefancikova, O. Champion, G. Laurent, A. Chateau, F. B. Hoch, F. Boschetti, F. Denat, S. Pinel, J. Devy, E. Porcel, S. Lacombe, R. Bazzi, S. Roux, *Int. J. Mol. Sci.* **2019**, *20*, 18.
- [53] Y. Li, J. S. Lee, *Materials (Basel)*. **2020**, *13*, 3093.
- [54] G. Maiorano, S. Sabella, B. Sorce, V. Brunetti, M. A. Malvindi, R. Cingolani, P. P. Pompa, *ACS Nano* **2010**, *4*, 12.
- [55] M. Kokkinopoulou, J. Simon, K. Landfester, V. Mailänder, I. Lieberwirth, *Nanoscale* **2017**, *9*, 8858.
- [56] N. Raval, R. Maheshwari, D. Kalyane, S. R. Youngren-Ortiz, M. B. Chougule, R. K. Tekade, in *Basic Fundamentals of Drug Delivery* (Ed: R. K. Tekade), Academic Press **2019**, Ch. 10, pp. 369–400.
- [57] J. J. G. Romera, jgromera/iapws., <https://zenodo.org/record/4744318>, (accessed: November 2021).
- [58] Y. Song, X. Zhao, Q. Tian, H. Liang, *Microfluid. Fundam. Devices Appl.* **2018**.
- [59] T. M. Squiers, S. R. Quake, *Rev. Mod. Phys.* **2005**, *77*, 3.
- [60] scikit-image.org, https://scikit-image.org/docs/stable/api/skimage.filters.html#skimage.filters.threshold_triangle, (accessed: October 2021).
- [61] E. Rogers, G. W. Zack, S. A. Latt, *J. Histochem. Cytochem.* **1977**, *25*, 7.
- [62] M. Anguiano, C. Castilla, M. Maška, C. Ederra, R. Peláez, X. Morales, G. Muñoz-Arrieta, M. Mujika, M. Kozubek, A. Muñoz-Barrutia, A. Rouzaut, S. Arana, J. M. Garcia-Aznar, C. Ortiz-de-Solorzano, *PLoS One* **2017**, *12*, 2.

- [63] C. N. Van Den Broek, R. A. A. Pullens, O. Frøbert, M. C. M. Rutten, W. F. Den Hartog, F. N. Van De Vosse, *Biorheology* **2008**, *45*, 651.
- [64] A. D. Edelstein, M. A. Tsuchida, N. Amodaj, H. Pinkard, R. D. Vale, N. Stuurman, *J. Biol. Methods* **2014**, *1*, 2.
- [65] J. C. Freedman, N. Sperelakis,
- [66] G. Benton, I. Arnaoutova, J. George, H. K. Kleinman, J. Koblinski, *Adv. Drug Deliv. Rev.* **2014**, *79*, 3.
- [67] D. Caballero, S. M. Blackburn, M. De Pablo, J. Samitier, L. Albertazzi, *Lab Chip* **2017**, *17*, 22.
- [68] R. K. Jain, L. L. Munn, D. Fukumura, *Nat. Rev. Cancer* **2002**, *2*, 4.
- [69] A. Nacev, S. H. Kim, J. Rodriguez-Canales, M. A. Tangrea, B. Shapiro, M. R. Emmert-Buck, *Int. J. Nanomed.* **2011**, *6*, 2907.
- [70] J. Rouwkema, B. F. J. M. Koopman, C. A. V. Blitterswijk, W. J. A. Dhert, J. Malda, *Biotechnol. Genet. Eng. Rev.* **2009**, *26*, 1.
- [71] P. Renz, M. Kokkinopoulou, K. Landfester, I. Lieberwirth, *Macromol. Chem. Phys.* **2016**, *217*, 17.
- [72] N. V. Konduru, R. M. Molina, A. Swami, F. Damiani, G. Pyrgiotakis, P. Lin, P. Andreozzi, T. C. Donaghey, P. Demokritou, S. Krol, W. Kreyling, J. D. Brain, *Part. Fibre Toxicol.* **2017**, *14*, 1.
- [73] R. Rampado, S. Crotti, P. Caliceti, S. Pucciarelli, M. Agostini, *Front. Bioeng. Biotechnol.* **2020**, *8*, 1.
- [74] O. Lieleg, R. M. Baumgärtel, A. R. Bausch, *Biophys. J.* **2009**, *97*, 6.
- [75] Z. Chen, F. Wang, J. Zhang, X. Sun, Y. Yan, Y. Wang, J. Ouyang, J. Zhang, T. Honore, J. Ge, Z. Gu, *Front. Bioeng. Biotechnol.* **2020**, *8*, 1.
- [76] C. S. Hughes, L. M. Postovit, G. A. Lajoie, *Proteomics* **2010**, *10*, 9.
- [77] K. I. W. Kane, E. Lucumi Moreno, C. M. Lehr, S. Hachi, R. Dannert, R. Sanctuary, C. Wagner, R. M. T. Fleming, J. Baller, *AIP Adv.* **2018**, *8*, 12.
- [78] E. A. Aisenbrey, W. L. Murphy, *Nat. Rev. Mater.* **2020**, *5*, 7.
- [79] M. Le Goas, F. Testard, O. Taché, N. Debou, B. Cambien, G. Carrot, J. P. Renault, *Langmuir* **2020**, *36*, 35.
- [80] W. J. McCarty, M. Johnson, *Biorheology* **2007**, *44*, 5.